CHEMISTRY OF MATERIALS

ARTICLE

pubs.acs.org/cm

Structure Determination and Compositional Modification of Body-Centered Tetragonal PX-Phase Lead Titanate

Jin Wang,*[,†] Kurt Schenk,[‡] Alexandra Carvalho,[†] Ben Wylie-van Eerd,[§] Joe Trodahl,[§] Cosmin S. Sandu,[†] Michel Bonin,[‡] Ivan Gregora,[⊥] Zhanbing He,[†] Tomoaki Yamada,[#] Hiroshi Funakubo,[#] Patrick R. Briddon,[¶] and Nava Setter[†]

[†]Ceramics Laboratory, EPFL—Swiss Federal Institute of Technology, 1015 Lausanne, Switzerland

[‡]Laboratory of Crystallography, EPFL—Swiss Federal Institute of Technology, 1015 Lausanne, Switzerland

[§]MacDiarmid Institute for Advanced Materials and Nanotechnology, Victoria University of Wellington, New Zealand

[⊥]Institute of Physics AS CR, Na Slovance 2, 182 21 Prague 8, Czech Republic

[#]Department of Innovative and Engineered Materials, Tokyo Institute of Technology, Nagatsuta-cho, Midori-ku, Yokohama 226-8502, Japan

[¶]School of Electrical, Electronic and Computer Engineering, University of Newcastle upon Tyne, Newcastle upon Tyne, NE1 7RU, United Kingdom

Supporting Information

ABSTRACT: The fibrous PX-phase of lead titanate (PT), which can be synthesized by a hydrothermal method, has been studied to clarify its structural aspects on the atomic level. By combining synchrotron X-ray diffraction and electron microscope analysis with a first-principles calculation, a unique open-channel structure with a 5.529 Å diameter bore through the whole wire is determined. First-principle modeling reveals that the PX-phase structure has an indirect wide band gap and a higher formation enthalpy than the tetragonal perovskite phase. Both the frequency and symmetry of Raman-active lattice vibrational modes have been identified with polarized Raman spectra on individual monocrystalline PX-phase PT wires, showing a good match with the first-principles calculation. Furthermore, the doping of Zr in the PX-phase PT and the influence on the structure were investigated, showing a limit of 17% incorporation of Zr in the PX-phase PT.

KEYWORDS: lead titanate, fibrous PX phase, structure determination, open channels, synchrotron X-ray, first-principles calculation, lattice vibration modes, Raman scattering, Zr doping

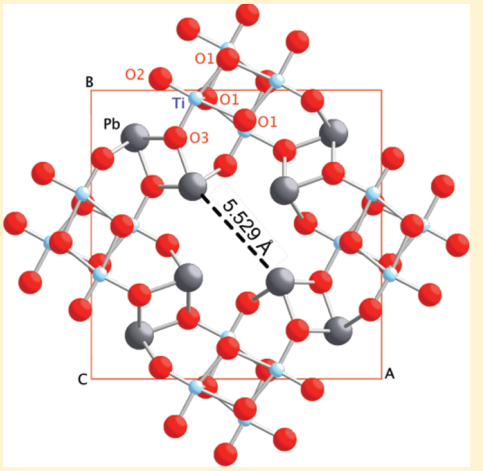

INTRODUCTION

The art of building different crystal structures with the same set of atoms has long been an interesting and productive activity. In particular, it is known that the various arrangements of the oxygen octahedra can be engineered to give several crystalline structures based on $PbTiO_3$ (PT)/$Pb(Zr,Ti)O_3$ (PZT). In perovskites, the best-known and extensively studied, corner-shared Ti—O octahedra are closely packed and have a relative flexibility of distortion and tilt under temperature changes or the application of an electric field or stress.[1] A defect-type pyrochlore with oxygen vacancies can also be crystallized with the $Pb_2Ti_2O_6$ formula (conventionally written as PT), in which oxygen-octahedra also share the corners but are packed relatively loosely.[2] Since as early as 1986 another structure has been reported by several groups[3,4] via the hydrothermal processing, showing the stoichiometry of $PbTiO_3$ but with a body-centered tetragonal structure differing from both the perovskite and the pyrochlore. Following ref 3, we denote it as the PX phase. A unique feature of the PX phase is that it seems to grow only in the form of fine acicular particles.[3−6] Interestingly and suggestively, the PX phase can be converted to perovskite phase by annealing without losing its acicular shape, making it a good precursor in the preparation of perovskite PT/PZT(Ti-rich) nanowires in large yield.[4,6]

The unique growth habit, permitting an interesting process for the preparation of perovskite nanowires, and the potentially interesting properties of the wires themselves entail the development of a deeper understanding of the PX phase. However, only a limited number of reports on its synthesis and microstructural characterization exist and even the crystalline structure of the PX phase has not been firmly established. We report here the structure of the PX phase, as determined by combining synchrotron X-ray diffraction and electron microscope analysis with first-principles modeling. Furthermore, polarized micro-Raman scattering spectra were measured on individual monocrystalline PX-phase wires and the symmetry of the Raman-active

Received: October 21, 2010
Revised: March 4, 2011
Published: April 20, 2011

normal modes was assigned according to the selection rules, showing a good agreement with first-principles calculations. Finally the solubility of Zr in the PX-phase PT and the influence of doping are investigated.

EXPERIMENTAL SECTION

Synthesis. The sample was prepared with a hydrothermal method similar to what is reported by Cheng et al..[4] For PX-phase PT, 4 mmol $Ti(OC_4H_9)_4$ was first dissolved in 8 mL of ethanol and the resulting transparent solution was hydrolyzed in 8 mL of deionized H_2O. Subsequently, 20 mmol of KOH, 5.2 mmol of $Pb(CH_3COO)_2 \cdot 3H_2O$, and 0.050 g of polyvinyl alcohol (PVA) were added and mixed under stirring. The volume of the final feedstock was adjusted to 40 mL with deionized H_2O. The ratio of Pb/Ti in the starting material was kept to 1.3 to ensure a complete reaction of $TiO_2 \cdot nH_2O$ gel. The 40 mL feedstock was transferred to a 50 mL Teflon-lined autoclave and held at 200 °C for 3.5 h. The products were washed with deionized H_2O until a neutral PH is achieved and then washed in 10 wt % CH_3COOH solution to remove the remnant PbO. The final pure PX-phase sample was obtained by another cycle of washing with deionized water and dried at 60 °C in air. For preparing the PX phase of Zr-doped PT, a designed ratio of $Zr(OC_3H_7)_4$ (70 wt % isopropanol solution) was mixed with $Ti(OC_4H_9)_4$ and dissolved in the 8 mL ethanol solution while the remaining operations were unchanged.

Microstructure Characterization. The morphology images and electron diffraction pattern were obtained by scanning electron microscopy (SEM, Philips XL 30) and transmission electron microscopy (TEM, Philips CM 300) equipped with a field emission gun at an accelerating voltage of 300 kV.

The cross-section sample preparation for the TEM was performed with the focused ion beam (FIB) technique (ZEISS NVision40) using a slightly modified in situ lift out procedure. The wires were dispersed on a TEM grid with carbon film. A micromanipulator needle (Kliendiek) was brought into contact with a wire. The wire was attached to the needle with a small C deposition at the contact point. After lifting off the wire from the grid it was then transferred to a TEM half-grid (Omniprobe) so that the wire was perpendicular to the grid surface. After attaching the wire with an electron beam induced C deposition (in order to avoid damage through the ion beam) the wire cross-section was then thinned down to electron transparency using a 30 kV ion beam in the beginning followed by a 5 kV cleaning step at the end in order to minimize the ion-beam-induced amorphous layer at the surface.

X-ray Crystallography. The powder diagram of the PX-phase PT has been collected twice. First measurements were made on a PANalytical MPD PRO laboratory instrument using Cu Kα radiation, then with synchrotron radiation at the Swiss-Norwegian beamline BM01B at the ESRF, Grenoble. A refinement on the Cu Kα pattern was seriously hampered by the high absorption factor. The synchrotron powder pattern was measured at a much shorter wavelength, and hence provided the necessary data quality for structure refinement. BM01B provides a beam of unfocused synchrotron radiation from a bending magnet source onto the sample contained in a 0.3 mm diameter capillary. A wavelength of 0.49836(1) Å was selected using a Si(111) channel-cut monochromator. The calibration of wavelength and the goniometer zero point of 0.0107 (8)° was made using a NBS640b silicon powder standard. An array of six Si(111) analyzer crystals was used to collect the room temperature powder diffraction pattern over an angular range $2.51° \leq 2\theta \leq 46.58°$ at intervals of 0.005°.

The powder diffraction spectra of Zr-doped PX phase were measured on a Bruker D8 ADVANCE diffractometer using Cu Kα radiation, with which the diffraction data of the PX-phase PT were also taken for comparison under the same instrumental parameters.

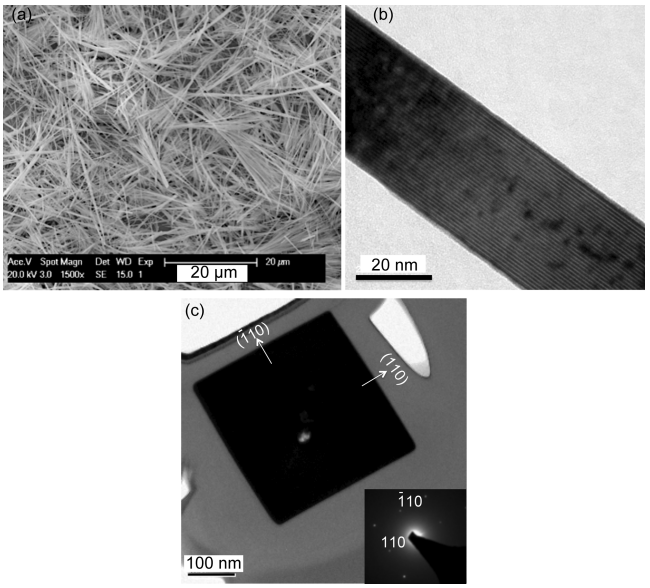

Figure 1. (a) SEM image of as-prepared PT. (b) TEM image shows the individual wires are monocrystalline. (c) The cross-section of the PX-phase wire and the orientations of its side surfaces.

Raman Spectra. The polarized Raman spectra of single PX-phase PT wires were taken with Renishaw RM-1000 with 514 nm laser on (100)-MgO substrate and Jobin Yvon T64000 in tripple monochromator mode with 488 nm laser on (0001)-sapphire substrate. A conventional backscattering mode with the incident laser beam perpendicular to the microscope stage was used and the laser spot was focused to 0.5−1 μm using a 100× or 50× objective. The wires were sparsely dispersed on the substrate and thus it was possible to capture part of a single wire as the Raman signal source.The laser power on the single wires is estimated ∼2 mW on the Renishaw RM-1000 system and <1 mW on the Jobin Yvon T64000 system. The spectra of the Zr-doped PX-phase PT were measured on the powder sample without a polarizer. The powder Raman spectrum of the PX-phase PT was also collected under similar conditions for comparison.

First-Principles Calculations. The PX-phase PT structure was modeled using a first-principles calculation. These were based on the density functional theory framework, as implemented in the AIMPRO code.[7] The local density approximation (LDA) for exchange-correlation functional (PW92)[8] was used along with the generalized gradient approximation (GGA) of Perdew, Burke and Ernzerhof (PBE)[9] for comparison.

The core electrons were treated using the dual space separable pseudopotentials of Hartwigsen, Goedecker and Hutter.[10] The semicore 3s and 3p electrons of Ti were treated among the valence electrons, although they were a posteriori not found to play a significant role in the bonding.

The valence wave functions on each atom by combinations are expanded in a basis of *s*, *p*, and *d* Cartesian Gaussian orbitals as described in ref 11. For each Pb, Ti and O atom four different Gaussian exponents were included. For O, four sets of s and p functions were included along with two d polarization functions (*ddpp*), whereas for Pb and Ti, all the four exponents included d functions (*dddd*). The exponents of the Gaussian functions were optimized by minimizing the energy of prototype cubic $PbTiO_3$, and convergence tests were carried out to ensure that the computed properties did not depend on the size of the basis set employed. For Mullikan charge populations, a lower number of basis functions per atom were used.

Periodic boundary conditions were imposed, and integrations over the Brillouin Zone (BZ) were carried out using a Monkhorst-Pack (MP)

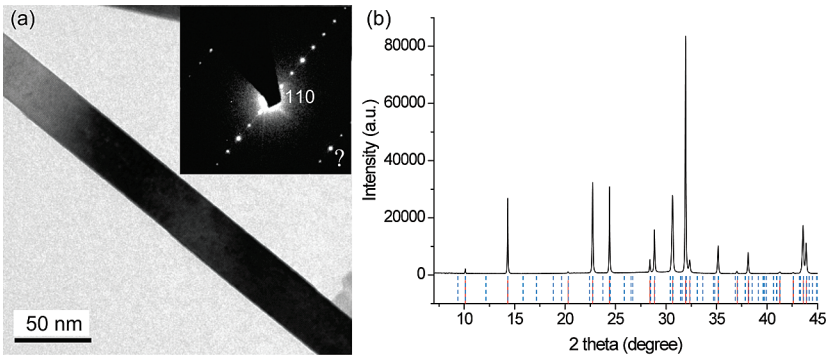

Figure 2. (a) TEM and electron diffraction pattern (inset) of a single PX-phase wire. (b) Measured XRD pattern (λ of X-ray source: 1.5406 Å) compared with the calculated peak positions from two sets of unit cells (dashed blue lines, calculated with the unit cell in ref 4; solid red lines, calculated with the unit cell after correction).

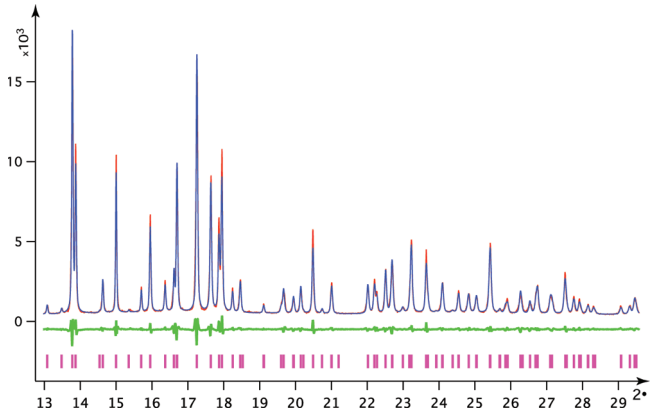

Figure 3. Typical part of the observed (red), computed (blue), and difference (green) profile from the Rietveld refinement at R_{wp} = 0.0793. Pink ticks represent reflection positions.

sampling scheme.[12] Converged grids were typically of 4 × 4 × 2 for structural optimization. The charge density was expanded using plane waves with a cutoff energy of 400 Ry.

The frequencies and normal coordinates of Raman-active modes are obtained directly by diagonalization of the dynamical matrix (using the 'Aimpro' code) and subsequent selection of the modes with the appropriate symmetry.

STRUCTURE DETERMINATION

The morphology of the PT product is seen in the SEM image of Figure 1a, in which only wires and wire bundles were observed. The thickness of the wires varies from 10 nm to more than 1 μm and the length from hundreds nm to over 100 μm. The XRD diffraction pattern of the product can be assigned to JCPDS 48−0105 reported by Cheng et al. within their measurement range. The similar preparation procedure and morphology and the closely fitted XRD pattern confirm that the product we prepared is the PX phase. The high-resolution TEM (Figure 1b,c) reveals that the individual PX-phase wires are monocystalline and have a square prism shape as shown by the cross section. The high variation of the contrast (the small bright area) in the cross-section sample (Figure 1c) is most probably due to the presence of the defects (dislocations) in this region. The variation of the contrast in this region decreases significantly when sample is slightly tilted away from the diffraction condition. Pores or holes have not been observed in the SEM images taken during the FIB preparation. Furthermore, such kind of defects was not observed during TEM investigations on nanowires dispersed on a TEM grid. The monocystalline nature of the individual wires has been also confirmed by synchrotron X-ray diffraction.[13]

The structure determination of this phase has been performed in two following steps: the redetermination of the unit cell and then the solution of the atomic structure. Cheng et al. have proposed a body-centered tetragonal unit cell of the PX phase with a = 12.358 Å and c = 14.541 Å.[4] However, we found contradictions with this identification in the analysis on the electron diffraction pattern obtained on the individual PX-phase wires, in which the angle correlations between crystal planes were exposed by the single-crystal diffraction pattern. For example, as shown in Figure 2a, with the assignment of (110) diffraction according to the unit cell proposed by Cheng et al., the diffraction plane shown with "?" which is perpendicular to (110) with an interplane displacement d of around 1.90 Å can not be satisfactorily indexed to any diffraction plane. In addition, a number of lines which could be allowed by this unit cell, commonly concerned with (h k l) peaks with $l \neq 0$ such as (101), (112), (002), and (202), are missing in the measured XRD pattern (Figure 2b), although this could be explained by the possibly weak intensity of these peaks or the existence of special positions. However, after a correction of the lattice constant c to 3.820 Å, a one-to-one match of peaks between the calculated (red lines in Figure 2b) and those measured is obtained. Both laboratory and synchrotron powder patterns could be readily indexed using the DICVOL program[14] in the redetermined unit cell given in Table 1. The diffraction spot with "?" in the electron diffraction (Figure 2a) can be readily identified as (002) diffraction. All the electron diffraction patterns taken by the authors can be indexed within the new unit cell.

With the redefined unit cell, it is shown that the PX-phase wires are directed along the c axis of the tetragonal cell with square facets on the {110} planes, indicated by the TEM image and the corresponding electron diffraction (Figures 1c and 2a).

The original model was found by the charge-flipping algorithm[15−17] on the Cu-data; some spurious atoms within the [001] channels quite conveniently disappeared when refining on the synchrotron profiles. The refinement was carried out with the help of the JANA system of program[16] (Figure 3). The final structure is shown in Figure 4 and the pertinent parameters may be found in Table 1.

The TiO_6-moieties build up columns of edge-shared octahedra that can be described by the idealized rod-group $P\bar{4}(2m)$ and the

dx.doi.org/10.1021/cm1030206 |Chem. Mater. 2011, 23, 2529–2535

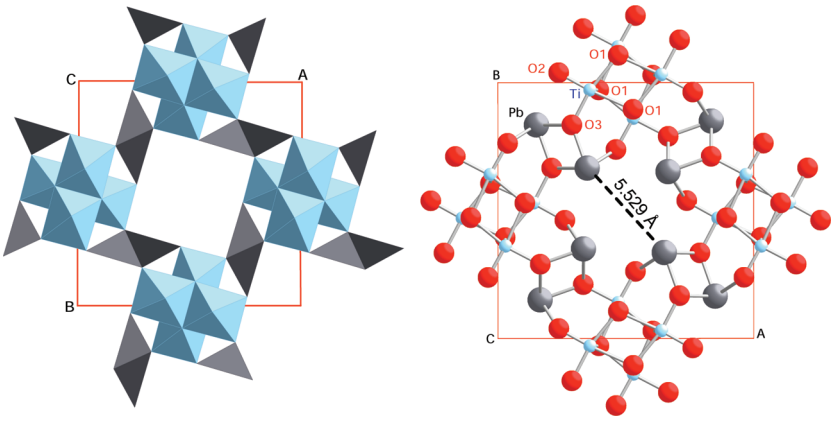

Figure 4. Structure of the PX phase: by means of polyhedra along the *c* axis (left), atom numbering and bore (right).

Table 1. Crystal Data (T = 293K) and Data Collection Specifics of PX-Phase $PbTiO_3$

M_r =303.1	R_p = 0.0616
Space Group $I4/m$	R_{wp} = 0.0793
a = 12.3853(1) Å	χ^2 = 2.48
c = 3.82000(4) Å	$\Delta\rho_{min}$, $\Delta\rho_{max}$ = 0.77, −0.66
V = 585.97(2) Å^3	D_X = 6.871 g cm^{-3}
Z = 8	D_m = 6.6 g cm^{-3} (He pycnometer)
λ= 0.49836(1) Å^{-1}	DEBYE-SCHERRER geometry
μ = 23.80 mm^{-1}	profile functions: Pseudo-VOIGT
R_F = 0.019	background function: 36 LEGENDRE-polynomials

PbO_5-moieties such of edge-shared pyramids of precise rod-group $P(11)2/m$. These columns connect in a corner-sharing manner to build up the 3D crystal edifice. [001] channels extend throughout the wires and the bore, measured as the shortest width of the channel, is 5.529 Å. This is a unique feature compared with the perovskite and pyrochlore phases. The Pb-pyramids are quite regular indeed, of which the equatorial Pb−O distances lie within 2.521(7) to 2.529(7) Å and the axial one is 2.274(14) Å. The lead atom extends out of the pyramid by −0.490 Å. The Ti-octahedron is less regular with Ti−O distances varying between 1.689(12) and 2.293(12) Å. The titanium atoms bend away from the center of the columns.

The refined lattice parameters are $a = b$=12.3853(1) Å and c = 3.82000(4) Å. The atomic coordinates are listed in Table 2.

The density of our prepared sample measured with Helium pycnometer is around 6.6 g/cm^3, consistent with 6.8 g/cm^3 measured with the specific gravity bottle method by Cheng et al.,[4] and both agree with the theoretical density 6.871 g/cm^3 of the structure.

It should be noted that very recently, Ren Z. H. et al.[18] reported an edge-shared-TiO_6 structure in $PbTiO_3$ nanosized tubes via hydrothermal process which could be possibly assigned to the PX phase, as signaled by the [001] growth direction and square shape in the outer profile of the cross-section of the tubes besides the similarity of the identified structure.

FIRST-PRINCIPLES STUDY ON THE PX-PHASE STRUCTURE

The structure geometry was optimized to minimize the total energy. Atomic positions (Table 2) were determined using a conjugate gradient algorithm, while the tetragonal lattice parameters a and c were found by simplex minimization. The calculated lattice parameters were a = 12.22 Å and c/a = 3.29 with the LDA and a = 12.52 Å and c/a = 3.30 with the GGA. This is in good agreement with the experimental values a = 12.39 Å and c/a = 3.24, having taken into account that LDA calculations usually underestimate the lattice volume, whereas GGA-PBE calculations usually overestimate it. The final structure keeps the $I4/m$ symmetry. In particular, the stability toward inversion-symmetry breaking perturbations was verified within a total energy accuracy of 0.001 eV.

Table 2. Fractional Atomic Coordinates of the PX Phase Obtained Experimentally and Optimized with the First-Principles Calculation[a]

	exp				calcd (PW92)		calcd (PBE)	
atom	x	y	z	U_{eq}	x	y	x	y
Pb	−0.33510(9)	0.65041(12)	0	0.0633(5)	−0.336	0.650	−0.349	0.668
Ti	−0.0312(3)	0.6426(4)	0	0.0598(18)	−0.032	0.644	−0.030	0.644
O1	0.1073(7)	0.5262(9)	0	0.051(4)	0.103	0.528	0.104	0.529
O2	0.0407(9)	0.7584(9)	0	0.056(4)	0.049	0.763	0.047	0.762
O3	−0.1639(12)	0.7168(8)	0	0.063(4)	−0.166	0.713	−0.164	0.713

[a] All the atoms lie on the Wyckoff position 8h of the $I4/m$ space group. U_{eq}: equivalent isotropic displacement parameters (Å^2) of the atoms.

The PX phase is less stable than the tetragonal perovskite ($P4mm$) phase. At 0 K and without applied pressure, there is an energy gain between 0.2 eV (PW92) and 0.3 eV (PBE) for the transformation of one primitive unit cell of PX into four tetragonal perovskite unit cells. The projection of the Kohn−Sham one electron states into Gaussian-type localized orbitals indicates that the PX phase is more covalent than the tetragonal perovskite phase. The static effective charges obtained from the Mullikan charge populations are respectively 1.6, 2.3, −1.7, −1.0, and −1.2 (in units of the electron charge) for Pb, Ti, O1, O2, and O3, lower than the calculated charges for the tetragonal perovskite using the same projectors (1.7, 3.3, −1.7, and −1.6 for Pb, Ti, and the two inequivalent oxygen atoms, respectively).

The PX phase has a larger LDA band gap energy (by 1.1 eV) than the tetragonal perovskite phase (which has a calculated LDA band gap of 1.5 eV, as typically obtained from pseudopotential calculations).[19] Similar to the latter, the PX phase has an indirect X-Γ band gap (See Figure S1 in the Supporting Information).

dx.doi.org/10.1021/cm1030206 |*Chem. Mater.* 2011, 23, 2529–2535

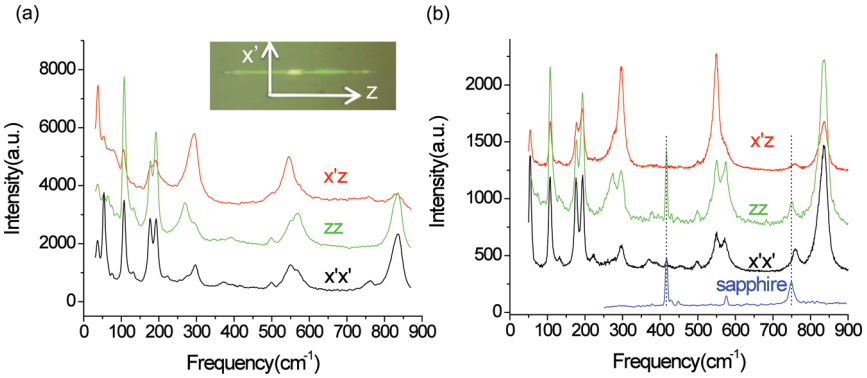

Figure 5. (a) Polarized Raman spectra taken from a single PX-phase wire with a 514 nm excitation laser and (100)-MgO substrate. (b) Polarized Raman spectra with a 488 nm excitation laser and the (0001)-sapphire substrate.

Table 3. Selection Rules for A_g, B_g, and E_g Modes under Three Different Polarization Configurations Adopted in the Measurement[a]

	$x'x'$	$x'z$	zz
A_g	V	I	V
B_g	V	I	I
E_g	I	V	I

[a] "V" and "I" indicate visible and invisible, respectively.

LATTICE VIBRATIONAL MODES AND RAMAN SPECTRA

The lattice vibration in such a unique structure is of great interest to study considering its relationship with the fundamental physical properties of the structure. As there are four formula units per primitive unit cell of the PX phase, the number of normal vibrational modes is $3 \times 4 \times 5-3=57$, from which 3 translational modes have been excluded. Knowing that all atoms in the PX structure occupy C_{1v} sites of the C_{4h}^5 $(I4/m)$ space group, the following zone-center lattice vibrational modes can be determined using site-symmetry analysis:[20] 10 A_g, 10 B_g, and 5 doubly degenerate E_g modes are Raman-active only; 4 A_u, 5 B_u, and 9 doubly degenerate E_u modes are infrared-active only (invisible in the Raman scattering).

The polarized micro-Raman technique, which can probe the Raman-scattering at the submicrometer size, offers an opportunity to determine the symmetries of the Raman-active lattice phonons in scattering from a single monocrystalline PX-phase wire. The Raman tensors for modes of A_g, B_g and E_g symmetry are given, in the coordinates referenced to the axes (a, b, c)

$$R(A_g) = \begin{bmatrix} a_1 & 0 & 0 \\ 0 & a_1 & 0 \\ 0 & 0 & a_2 \end{bmatrix} \quad R(B_g) = \begin{bmatrix} b_1 & b_2 & 0 \\ b_2 & -b_1 & 0 \\ 0 & 0 & 0 \end{bmatrix}$$

$$R(E_g) = \begin{bmatrix} 0 & 0 & e_1 \\ 0 & 0 & e_2 \\ e_1 & e_2 & 0 \end{bmatrix}, \begin{bmatrix} 0 & 0 & -e_2 \\ 0 & 0 & e_1 \\ -e_2 & e_1 & 0 \end{bmatrix}$$

In conventional backscattering mode, the available polarizations on a wire lying flat on a substrate are along the wire and perpendicular to it, so along the c axis and some direction in the (001) plane; we label these as z and x', respectively (see Figure 5). It is important that in the absence of knowledge concerning the rotational orientation of the wires, x' corresponds to an unspecified direction in the crystallographic (001) plane. In the usual Porto notation the available polarizations are $x'x'$, zz and zx' (or equivalently $x'z$), in which the two letters denote the incident and scattered

Table 4. Comparison between the Frequencies and Symmetry of the Raman-Active Vibration Modes Obtained with First-Principles Calculation and Measured by Polarized Raman Scattering on a Single PX-Phase PT Wire[a]

calcd		exp	
freq (cm^{-1})	symmetry	freq (cm^{-1})	symmetry
831	A_g	837	A_g
748	B_g	761	B_g
684	B_g		
609	A_g	573	A_g
586	E_g	550	E_g
507	A_g	499	A_g
457	B_g	457	B_g*
430	B_g		
407	A_g	392	A_g*
388	B_g	370	B_g
299	E_g	297	E_g
289	A_g	274	A_g
282	B_g		
281	E_g		
276	A_g*		
235	B_g*	224	B_g
217	A_g	193	A_g
194	B_g*		
192	E_g		
177	A_g	178	A_g
112	A_g	107	A_g
104	B_g	134	B_g*
64	B_g	56	B_g
62	A_g		
43	E_g	37	E_g

[a] The symbol "*" indicates a mode symmetry that is determined with a low degree of certainty.

dx.doi.org/10.1021/cm1030206 |Chem. Mater. 2011, 23, 2529–2535

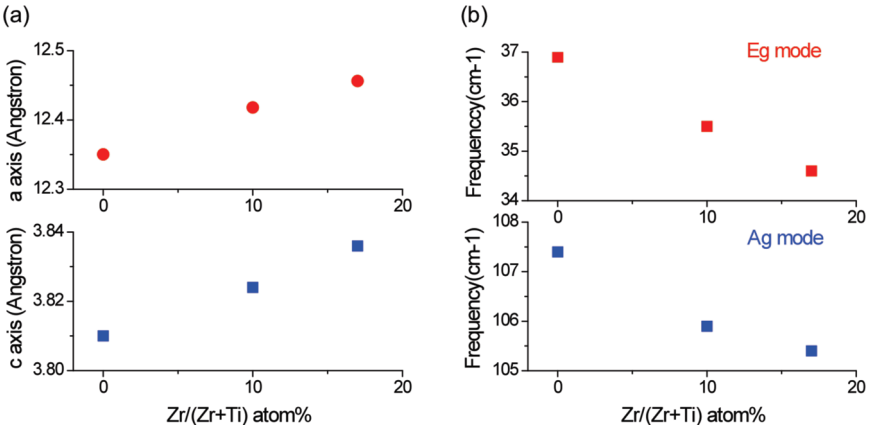

Figure 6. (a) Quantitative correlation between the unit-cell parameters of the tetragonal unit cell and the composition of the PX phase. (b) Frequency shift in the Raman as a function of the composition of the PX phase.

polarization directions, respectively. The Raman tensors then imply immediately the polarization selection rules listed in Table 3. However, in the following paragraph, we show that the measured spectra are of mixed polarization, leading to significant cross talk between the polarization selections. The laser spot was focused to 0.5−1 μm using a 100× or 50× objective with numerical apertures of 0.9 and 0.7, respectively. In all cases, the wires then filled only a small fraction of the illuminated spot, so it was necessary to use substrates with well-characterized Raman signals for which the measured data could be corrected. Uncertain corrections for second order substrate scattering and low-density secondary phases prevent the reliable assignment of weak signals to the wires.

The wires that were aligned coincidently (or intentionally aligned with the controlled rotation of the microscope stage) parallel to the polarization axis of the incident beam were measured under three different polarization configurations, $x'x'$, $x'z$, and zz. Note that for strong focusing the polarization at the focus is somewhat scrambled with respect to the polarization of the laser beam or (more seriously) the light at the analyzer set in front of the monochromator, so some degree of cross talk between the various polarizations can be expected. In addition the large angular range of propagation directions at the focus, approximately ±25°, prevents the unique specification of the incident and scattered propagation direction that is possible with well-collimated optics. The scrambling of both the polarization and propagation directions is severely exacerbated by focusing on a nonplanar surface such as the present nanowires. Thus we omit entirely any specification of propagation direction in our Porto notation of the scattering configuration, and note further that the selection rules of Table 3 are only approximately obeyed. Nonetheless the spectra show polarization-dependent line strengths which permit the assignment of vibrational symmetry (A_g, B_g, E_g) for all of the lines we observe.

Figure 5a shows the Raman spectra taken under $x'x'$, $x'z$, and zz polarization configurations from a single PX-phase wire with a 514 nm excitation laser and 50× (NA = 0.7) objective on wires lying on a (100)-MgO substrate, whereas Figure 5b represents the results with a 488 nm excitation laser, 100× (NA = 0.9) and the (0001)-sapphire substrate. Polarization scrambling leads to the appearance of some lines in forbidden polarization spectra, especially severe in the data taken with the NA=0.9 objective. In view of the polarization scrambling in a microscope we have treated "invisible" in Table 3 to be interpreted as "weak" in the identification of the mode symmetry in the measured scattering spectra. The resulting mode-symmetry assignments are listed in Table 4. The modes at 392, 457, and 134 cm^{-1} are determined with a low degree of certainty indicated with an asterisk "*", as their symmetry could not be unambiguously assigned.

The Raman-active phonon frequencies and the corresponding symmetry obtained from first-principles calculation are also listed in Table 4 for comparison. It is seen that both the frequencies and symmetries of the modes which are identified in the polarized Raman scattering agree well with the calculated ones, which further confirms the validity of the proposed structure of the PX phase. It is not unusual that not all the predicted modes were observed. As the symmetry arguments tell nothing about the intensity, it often happens that some modes allowed by the selection rule are too weak to be detectable in practice.[21]

ZR-DOPED PX-PHASE PT

To get the Zr-doped PX-phase PT, a set of fabrication experiments with different atomic ratios of Zr/(Zr+Ti) (10, 20, and 30 at %) in the starting materials were carried out. All the products have the wire morphology (Figure S2 in the Supporting Information) and are confirmed to be PX phase by powder XRD (Figure S3 in the Supporting Information). The samples obtained with the starting gel of 10 and 20 at % Zr/(Zr+Ti) show an increase of the lattice constants, signaling that Zr^{4+} is inserted into the lattice (see Figure S4 in the Supporting Information). The sample prepared with the 30 at %-Zr/(Zr+Ti) starting gel shows no further increase in the unit-cell size (see Figure S4 in the Supporting Information). A composition analysis with energy dispersive spectra (EDS) of TEM reveals that the real concentrations of Zr in the lattice are 10, 17, and 17 at % in Zr/(Zr+Ti) in the samples prepared with the starting gel with Zr/(Zr+Ti)=10, 20, and 30 at % respectively (see Figure S5 in the Supporting Information). More Zr-rich amorphous phase was observed by TEM in the nominal 30 at %-Zr/(Zr+Ti) sample. The existence of the maximum Zr-doping level probably suggests a limit of the solubility of Zr in the PX-phase $PbTO_3$ lattice at around 17 at % of Zr/(Zr+Ti).

Figure 6a shows the quantitative correlation between the unit-cell parameters of the tetragonal unit cell (a and c axis are extracted from (330) and (002) peaks in the powder diffractions) and the composition. It is seen that both a and c axis change linearly with the Zr doping concentration, following the Vegard's law for the change

dx.doi.org/10.1021/cm1030206 |Chem. Mater. 2011, 23, 2529–2535

of unit cell size in the solid solution formed by substitution. The influence of the doping with Zr is also reflected in the Raman spectra. Figure 6b shows the shifts of the Eg mode (at about 37 cm^{-1}) and Ag mode (at about 107 cm^{-1}), both toward the lower frequency, as examples. This red shift, which occurs generally in all observed Raman modes, results from a combination of the substitution of Ti with heavier Zr atoms and a reduced stiffness of at least some modes in the expanded lattice. The increasing effective mass of vibrations in which the Ti ions participate alone would lead to a frequency reduction in purely Ti-ion vibrations of 4.2% (6.8%) in material with Zr concentrations of 10 at % (17 at %). This is the order of the strongest softening measured.

The increase in the unit cell is expected, as octahedrally coordinated Zr^{4+} possesses an ionic radius (0.86 Å) larger than octahedrally coordinated Ti^{4+} (0.75 Å). The larger ionic radius imposes a barrier for Zr^{4+} to substitute Ti^{4+}. It is known that the substitution of Ti^{4+} with Zr^{4+} in the perovskite $PbTiO_3$ is up to 100% even in the hydrothermal synthesis of perovskite PZT powders at the similar temperature,[22] whereas the doping with Zr in the PX- phase $PbTiO_3$ is shown to be quite limited. This could be related to the kinetics of the growth. The substitution of Zr in the PX-phase PT causes an expansion of the O octahedra in three dimensions as shown by the increase of the three principal axes of the unit cell upon doping with Zr. On the other hand, in the perovskite PT, the induced expansion of the octahedra by Zr takes place only in two dimensions as indicated by the increase of *a* axis and the approximate invariance of *c* axis.[23] This is also reflected by that the three diagonal O−O distances in the O octahedra in the PX-phase PT structure are 3.82, 3.97, and 4.10 Å, whereas 3.90, 3.90, and 4.15 Å in the perovskite PT (JCPDS 06−0452). Assuming that the formation of PX-phase PT always occurs first during the growth of the PX-phase PZT, the higher energy barrier of substitution of Ti^{4+} with Zr^{4+} in the PX-phase PT relative to that in the perovskite PT could thus hinder the sufficient incorporation of Zr^{4+} in the lattice.

CONCLUSION

A unique open-channel structure with a 5.529 Å bore size through the whole wire, supported by X-ray diffraction, first-principles calculations and Raman spectroscopy experiments, has been determined for the PX-phase lead titanate. First-principles modeling reveals that the PX-phase structure has an indirect wide band gap and a higher formation enthalpy than the tetragonal phase. The Raman-active lattice vibrational modes have been identified with polarized Raman spectra on the single PX-phase PT wire, indicating a good match with the first-principles calculation. It is also shown in this work that the family of the PX phase can be expanded by doping with Zr and the resultant structure is obviously affected by the doping, although there seems an upper limit on the doping level in the PX-phase PT lattice. The doping can thereby possibly adjust the channel width and other physical properties. The 1D growth habit of the PX phase should be closely related to the large portion of vacant space on the (001) plane leading to a substantially higher surface energy of this plane. The molecule-sized nanochannels may find some applications in the selective absorption and catalysis, sensing and storage, etc.

ASSOCIATED CONTENT

Supporting Information. Crystallographic information in CIF format; additional figures (PDF). This material is available free of charge via the Internet at http://pubs.acs.org.

AUTHOR INFORMATION

Corresponding Author
*E-mail: jin.wang@epfl.ch.

ACKNOWLEDGMENT

Jin Wang, Alexandra Carvalho, and Nava Setter acknowledge the Swiss National Science Foundation and the EU (NoE MIND on piezoelectricity) for financial support. The authors express their gratitude to the Swiss-Norwegian beamline consortium for providing access to synchrotron radiation, and to Dr P. Pattison for collecting the experimental data. CIME (electron microscopy center of EPFL) is acknowledged for generously allowing us to use their facilities. Support from the Project KAN301370701 of the Academy of Sciences of the Czech Republic is also acknowledged.

REFERENCES

(1) Setter, N.; Colla, E. L., Eds. *Ferroelectric Ceramics*; Ceramics Lab: Lausanne, Switzerland, 1993.
(2) Ju, J.; Wang, D. J.; Lin, J. H.; Li, G. B.; Chen, J.; You, L. P.; Liao, F. H.; Wu., N. Z.; Huang, H. Z.; Yao, G. Q. *Chem. Mater.* **2003**, *15*, 3530.
(3) Uedaira S.; Suzuki M.; Yamanoi H.; Tamura H. Eur. Pat. Appl. No. EP 186199, July 1986.
(4) Cheng, H. M.; Ma, J. M.; Zhao, Z. G.; Qiang, D.; Li, Y. X.; Yao, X. *J. Am. Ceram. Soc.* **1992**, *75*, 1123.
(5) Rujiwatra, A.; Thammajak, N.; Sarakonsri, T.; Wongmaneerung, R.; Ananta, S. *J. Cryst. Growth* **2006**, *289*, 224.
(6) Wang, J.; Sandu, C. S.; Setter, N. *IEEE Trans. Ultrason. Ferroelectr. Freq. Contr.* **2009**, *56*, 1813.
(7) Briddon, P. R.; Jones, R. *Phys. Status Solidi* **2000**, *217*, 131.
(8) Perdew, J. P.; Wang, Y. *Phys. Rev. B* **1992**, *45*, 13244.
(9) Perdew, J. P; Burke, K.; Ernzerhof, M. *Phys. Rev. Lett.* **1996**, *77*, 3865.
(10) Hartwigsen, C.; Goedecker, S.; Hutter, J. *Phys. Rev. B* **1998**, *58*, 3641.
(11) Goss, J. P.; Shaw, M. J.; Briddon, P. R. *Top. Appl. Phys.* **2007**, *104*, 69.
(12) Monkhorst, H. J.; Pack, J. D. *Phys. Rev. B* **1976**, *13*, 5188.
(13) Yamada, T.; Wang, J.; Sakata, O.; Sandu, C. S.; He, Z. B.; Kamo, T.; Yasui, S.; Setter, N.; Funakubo, H. *J. Euro. Ceram. Soc.* **2010**, *30*, 3259.
(14) Boultif, A.; Louër, D. *J. Appl. Crystallogr.* **2004**, *37*, 724.
(15) Oszlányi, G.; Sütö, A. *Acta Crystallogr., Sect. A* **2004**, *60*, 134.
(16) Petříček, V.; Dušek, M.; Palatinus, L. *Jana2006 Structure Determination Software Programs*; Institute of Physics: Praha, Czech Republic, 2006.
(17) Palatinus, L.; Chapuis, G. *J. Appl. Crystallogr.* **2007**, *40*, 786.
(18) Ren, Z. H; Xu, G.; Liu, Y.; Wei, X.; Zhu, Y. H.; Zhang, X. H.; Lv, G. L.; Wang, Y. W.; Zeng, Y. W.; Du, P. Y.; Weng, W. J.; Shen, G.; Jiang, J. Z.; Han, G. R. *J. Am. Chem. Soc.* **2010**, *132*, 5572.
(19) Hosseini, S. M.; Movlarooya, T.; Kompany, A. *Phys. B: Condens. Matter* **2007**, *391*, 316.
(20) Rousseau, D. L.; Bauman, R. P.; Porto, S. P. S. *J. Raman Spectrosc.* **1981**, *10*, 253.
(21) Long, D. A. *Raman Spectroscopy*; McGraw-Hill: London, 1977.
(22) Lencka, M. M.; Anderko, A.; Riman, R. E. *J. Am. Ceram. Soc.* **1995**, *78*, 2609.
(23) Kutty, T. R. N.; Balachandran, R. *Mater. Res. Bull.* **1984**, *19*, 1479.